

Optical and orbital characterization of spherically symmetric static black holes of self-gravitating new nonlinear electrodynamics model

İlim İrfan Çimdiker,^{1,2, a} Ali Övgün,^{3, b} and Yosef Verbin^{2, c}

¹*Institute of Physics, University of Szczecin,
Wielkopolska 15, 70-451 Szczecin, Poland*

²*Astrophysics Research Center, the Open University of Israel, Raanana 4353701, Israel*

³*Physics Department, Eastern Mediterranean University,
Gazimagusa 99628 via Mersin 10, Turkiye*

(Dated: March 12, 2026)

Horizon scale imaging and precision lensing have turned black holes into quantitative laboratories for strong gravity and for non standard electromagnetic physics. We study the optical appearance and orbital dynamics of a new class of static spherically symmetric black holes sourced by a Palatini inspired nonlinear electrodynamics model, minimally coupled to Einstein-Hilbert gravity. Using a unified geodesic analysis, we identify the key radii that organize the strong field phenomenology. For photons we determine the unstable photon sphere, the associated critical capture threshold, and the resulting shadow size for a distant observer, and we map how these observables respond to the charge and to the nonlinearity index n . For massive probes we compute circular orbits and the innermost stable circular orbit, clarifying the departure from the Schwarzschild and Reissner-Nordström cases. We then connect to classical tests by evaluating the light deflection angle and periastron advance, providing additional diagnostics that complement the shadow. Our results furnish a practical reference model for confronting first order nonlinear electrodynamics black holes with current and forthcoming imaging and lensing data.

PACS numbers: 95.30.Sf, 04.70.-s, 97.60.Lf, 04.50.Kd

Keywords: Black holes; Nonlinear electrodynamics; Light deflection; Shadows; Particle orbits.

I. INTRODUCTION

Black holes (BHs) provide an unparalleled arena to confront general relativity (GR) with observations in the strong-field regime. The past decade has witnessed a qualitative shift from indirect evidence to horizon-scale probes: precision astrometry of stellar orbits around Sgr A* has revealed

^a ilim.cimdiker@phd.usz.edu.pl

^b ali.ovgun@emu.edu.tr

^c verbin@openu.ac.il

relativistic orbital precession consistent with GR expectations [1], while the Event Horizon Telescope (EHT) has delivered horizon-scale images of the shadow-casting region of M87* and Sgr A* [2, 3]. Complementary frameworks have developed the use of horizon-scale imaging and strong-field electromagnetic probes to test the Kerr hypothesis and constrain non-GR deformations across a broad class of scenarios, including parameterized metrics and environment-sensitive shadow models [4–14]. These developments motivate a systematic exploration of how beyond-GR effects and non-standard matter sectors can imprint themselves on null geodesics, photon regions, lensing observables, and shadow morphology, thereby enabling model selection (or exclusion) with increasing observational leverage. Recent work argues that “spacetime collisions” can exhibit a distinctly electrodynamic character, motivating strong field tests that treat electromagnetic nonlinearities as dynamical players rather than small corrections [15].

From a theoretical standpoint, BH shadows encode the boundary between captured photon trajectories and those reaching a distant observer. In asymptotically flat spacetimes this boundary is closely tied to critical impact parameters and the structure of photon spheres or photon regions [16–18]. In parallel, gravitational lensing in both weak and strong deflection regimes provides complementary observables, including deflection angles, relativistic images, and time delays, whose analytic characterization has proven especially powerful for discriminating between nearby spacetimes [19–23]. The modern literature emphasizes that, beyond the idealized “shadow” of geometric optics, observable features such as photon rings and lensing rings depend on astrophysical emission models; nevertheless, the underlying geometric criticality remains a robust diagnostic of the metric in the near-horizon region [17, 24]. A concrete example in this direction is the rotating Einstein-Euler-Heisenberg black hole, where nonlinear electrodynamics modifies both the shadow morphology and the quasinormal mode spectrum in a correlated way [25]. Related analyses of nonlinearly charged black holes connect horizon scale imaging with accretion physics by jointly modeling the shadow and thin disk observables across the model parameter space [26].

A particularly well-motivated class of departures from the Einstein–Maxwell paradigm arises when the electromagnetic sector is promoted to a nonlinear electrodynamics (NLED) theory. Historically, NLED was introduced to regularize diverging classical fields and self-energies (as in Born–Infeld electrodynamics) and it also appears as an effective description of quantum vacuum polarization in strong fields (Euler–Kockel–Heisenberg), thereby providing a controlled framework for strong-field phenomenology [27–30]. Complementary frameworks have developed the use of horizon-scale imaging and strong-field electromagnetic probes to test the Kerr hypothesis and constrain non-GR deformations across a broad class of scenarios, including parameterized metrics and

environment-sensitive shadow models [4–14]. When coupled to gravity, NLED can significantly modify black-hole spacetimes and their causal/optical structure [31–34], and in particular it can support regular (non-singular) geometries, as famously demonstrated by the interpretation of the Bardeen spacetime within Einstein–NLED [35–42]. Regular/NLED-supported solutions and their generalizations have also been constructed in broader settings, including higher-dimensional and Lovelock gravities and related nonlinear Maxwell sectors, enlarging the space of analytic strong-field templates beyond four-dimensional Einstein–Hilbert theory [43–46]. Beyond regularity, NLED theories exhibit additional structural features, including electric–magnetic duality rotations and $SL(2, \mathbb{R})$ -type invariances in axion–dilaton extensions, which further enrich their gravitational sector [47, 48]. Moreover, NLED light propagation is governed by an effective optical geometry, so that NLED light rays can deviate from metric null geodesics, inducing characteristic corrections to lensing and shadow observables [49, 50]. These optical effects have direct phenomenological counterparts in lensing/shadow studies of Born–Infeld-type black holes and plasma-modified propagation, strengthening the link between NLED microphysics and observable ray-tracing signatures [51, 52]. Moreover, the regularity program has been extended to rotating spacetimes and to alternative constructions where NLED fields source nonsingular rotating black holes, with corresponding implications for photon regions and shadow shapes [53–57]. These motivations become even sharper in the EHT era: horizon-scale imaging of M87* and Sgr A* provides direct constraints on non-Einsteinian/charged compact-object scenarios [2, 3, 58], with dedicated analyses showing that the 2017 EHT data can bound effective charges and related couplings [59, 60] and that magnetically charged/NLED black holes can be confronted with EHT measurements [61]. In parallel, analytic developments have clarified the relation between the shadow edge, photon rings, and lensing rings as robust probes of near-horizon geometry [17, 24, 62], while recent studies emphasize that NLED effects can imprint coherently across several channels such as; shadows, deflection angles, quasinormal spectra, and greybody factors, enabling multi-observable consistency tests [63, 64]. Related model-building directions include NLED coupled to modified-gravity sectors (e.g. Palatini $f(R)$ or $f(R)$ -NLED realizations), as well as other regularization mechanisms such as higher-curvature (quadratic) gravity, which collectively broaden the landscape of nonsingular compact objects worth confronting with strong-field observables [65–69].

In this context, recently a new family of nonlinear gauge-field theories has been constructed by adopting a first-order (Palatini-inspired) formulation for linear and nonlinear electrodynamics, in which the field strength and potential are treated as a priori independent variables [70, 71]. Within this framework, Verbin *et al.* [71] obtained new self-gravitating solutions, including spherically

symmetric black holes, and identified a “Palatini Inspired NLED” (PINLED) model as a minimal and analytically tractable representative exhibiting novel features in both flat space and in the self-gravitating case. Since the phenomenological discriminant power of such solutions ultimately hinges on observables, it is timely to develop a detailed optical and orbital characterization of these geometries.

The aim of this paper is to provide a systematic analysis of the gravitational optics and kinematics of the static, spherically symmetric black-hole solutions of a family of PINLED models minimally coupled to Einstein–Hilbert gravity. Concretely, we (i) determine the photon sphere structure and the associated critical impact parameter controlling capture versus escape; (ii) compute the shadow radius as perceived by an observer at infinity and map its dependence on the NLED charge and the nonlinearity index n ; and (iii) complement these horizon-scale diagnostics with classical tests such as light deflection and periastron precession, enabling cross-validation against both weak field and strong-field constraints. Our results are presented in a form suited for direct comparison with the Schwarzschild (S) and Reissner-Nordström (RN) limits, and for integration into broader frameworks that confront modified-gravity/NLED scenarios with EHT and lensing data [2, 3, 19, 59, 60].

Beyond furnishing concrete predictions for a new analytic family of NLED black holes, the broader importance of this work is methodological and phenomenological: it illustrates how first-order NLED constructions translate into sharp optical signatures, and it strengthens the bridge between model-building in strong-field gravity and the rapidly maturing observational program targeting horizon-scale structure. As data quality improves, such theoretically controlled templates will be essential for turning shadow and lensing measurements into precision tests of fundamental physics.

II. PINLED BLACK HOLES

The Palatini inspired variant of NLED (PINLED) stands on the basic principle that a theory of vector field may be constructed in terms of a gauge potential A_μ and an anti-symmetric tensor field $P_{\mu\nu}$ which are independent of each other. The theory is of first order in the sense that the Lagrangian contains only first derivatives of A_μ through the gauge invariant combination $F_{\mu\nu} \equiv \partial_\mu A_\nu - \partial_\nu A_\mu$ (or $F \equiv dA$). In order to obtain the field equations of the theory, the dynamical variables A_μ and $P_{\mu\nu}$ are varied independently of each other.

This is actually a family of Lagrangians which are determined by an arbitrary *defining function*

of the first 4 of the 6 scalars which may be constructed as bilinear products of $F_{\mu\nu}$ and $P_{\mu\nu}$ and their duals $*F^{\mu\nu} = \epsilon^{\mu\nu\rho\sigma} F_{\rho\sigma}/2\sqrt{-g}$ and $*P^{\mu\nu}$ (defined analogously):

$$Y = P^{\mu\nu} F_{\mu\nu} , \quad Z = P^{\mu\nu} P_{\mu\nu} , \quad \Upsilon = F_{\mu\nu} *P^{\mu\nu} , \quad \Omega = P_{\mu\nu} *P^{\mu\nu} , \quad X = F^{\mu\nu} F_{\mu\nu} , \quad \Xi = F_{\mu\nu} *F^{\mu\nu} . \quad (2.1)$$

We write therefore the Lagrangian density (J^μ is a possible current):

$$\mathcal{L}_{\text{PINLED}} = \mathcal{K}(Z, \Omega, Y, \Upsilon) - J^\mu A_\mu , \quad (2.2)$$

which gives rise to the following field equations:

$$-2\nabla_\mu (\mathcal{K}_Y P^{\mu\nu} + \mathcal{K}_\Upsilon *P^{\mu\nu}) = J^\nu , \quad 2(\mathcal{K}_Z P^{\mu\nu} + \mathcal{K}_\Omega *P^{\mu\nu}) + \mathcal{K}_Y F^{\mu\nu} + \mathcal{K}_\Upsilon *F^{\mu\nu} = 0 . \quad (2.3)$$

The defining function is of course not entirely arbitrary, but must obey some physical constraints. The conventional practice in the first order formulation of NLED is to impose the condition that the first order theory with the defining function $\mathcal{K}(Z, \Omega, Y, \Upsilon)$ is equivalent to a certain 2nd order NLED theory [71, 72]. However, the new PINLED family is a wider family of NLED Lagrangians free of this limiting constraint [70, 71].

As mentioned above, there are still physical constraints to be fulfilled, but we will not deviate here for a full study of this issue. We will specify only one example which is the existence of the Maxwell limit. This will be evidently the case in the simple PINLED Lagrangian which we choose to study here from now on. In this Lagrangian the nonlinearity originates from the Y^n term of the otherwise linear defining function $\mathcal{K}(Z, \Omega, Y, \Upsilon) = Z/4 - Y/2 + \gamma Y^n/(2n)$. More explicitly, we write the Lagrangian of the ‘‘PINLED Y^n model’’ (or ‘‘ Y^n model’’ for short) as

$$\mathcal{L}_{Y^n}^{(1)} = \frac{1}{4} P^{\mu\nu} P_{\mu\nu} - \frac{1}{2} P^{\mu\nu} F_{\mu\nu} + \frac{\gamma}{2n} (P^{\mu\nu} F_{\mu\nu})^n - J^\mu A_\mu , \quad (2.4)$$

where γ is a real parameter. It is clear that for $\gamma = 0$, this reduces to the 1st order version of Maxwell’s theory and $P_{\mu\nu} = F_{\mu\nu}$.

Now, variations with respect to A_μ and $P_{\mu\nu}$ give the modified source-full ‘‘Maxwell’’ equations and the P - F relations:

$$\nabla_\mu (W(Y) P^{\mu\nu}) = J^\nu , \quad P_{\mu\nu} = W(Y) F_{\mu\nu} , \quad \text{where } W(Y) \equiv 1 - \gamma Y^{n-1} . \quad (2.5)$$

Now we add the Einstein-Hilbert term $R/2\kappa$ to the Y^n -Lagrangian for allowing a dynamical gravitational field which solves the Einstein equations

$$G_{\mu\nu} = -\kappa T_{\mu\nu} , \quad T_{\mu\nu} = -W^2 F_{\mu\alpha} F_\nu{}^\alpha - \frac{g_{\mu\nu}}{2} \left[\frac{n-2}{2n} W - \frac{n-1}{n} \right] Y . \quad (2.6)$$

Next we assume spherically-symmetric electrostatic solutions of the field equations (2.5)–(2.6). This means that the only non-vanishing field components are $F_{tr}(r) = -F_{rt}(r)$ and $P_{tr}(r) = -P_{rt}(r)$ and the metric tensor can be written in the form $g_{\mu\nu} = \text{diag}(f(r), -1/f(r), -r^2, -r^2 \sin^2 \theta)$. The NLED field equations can be solved analytically for F_{tr} and P_{tr} in parametric form with the variable Y in the role of the parameter [71]:

$$\begin{cases} F_{tr} = \sqrt{-Y/2W(Y)} \ , \quad P_{tr} = \sqrt{-W(Y)Y/2} \\ r = \left(\frac{2Q^2}{-YW^3(Y)} \right)^{1/4} \end{cases} \quad (2.7)$$

Notice that for electric fields $Y \leq 0$. The energy-momentum components of this electrostatic solution can be obtained from the expression for T_μ^ν in (2.6) as:

$$T_r^r = T_0^0 = -\frac{1}{4}Y + \frac{3n-2}{4n} \gamma Y^n \quad , \quad T_\theta^\theta = T_\varphi^\varphi = \frac{1}{4}Y + \frac{n-2}{4n} \gamma Y^n, \quad (2.8)$$

and their r -dependence can be obtained exactly as in Eq. (2.7). We observe that the energy density is positive definite as long as $(-1)^n \gamma > 0$ which is the assumption we will take from now on.

This solution (2.7) has the same form in flat spacetime as well. For further details we refer the reader to Ref. [71] and note here only that the electric field does not diverge as $r \rightarrow 0$. For $n = 2$, $F_{tr}(0)$ is finite, while for all $n \geq 3$ it is zero. The total field energy is always finite.

For the next stages of the discussion it will be much more convenient to transform to dimensionless quantities: the electric components will be rescaled with a parameter \mathfrak{E} which has units of electric field, defined by $|\gamma| = 1/\mathfrak{E}^{2(n-1)}$ and the quantities with dimensions of length like r , M and Q will be rescaled by the length parameter $\ell = 1/\sqrt{\kappa\mathfrak{E}^2}$, such that $\varrho = r/\ell$, $m = M/\ell$ and $q = \kappa\mathfrak{E}Q$. Within this dimensionless framework we will write the dimensionless, static, spherically symmetric metric in terms of the single free (lapse) function $f(\rho)$ as

$$ds^2 = f(\rho) dt^2 - \frac{1}{f(\rho)} d\rho^2 - \rho^2 (d\theta^2 + \sin^2 \theta d\phi^2). \quad (2.9)$$

For such a metric, Einstein's equations reduce to a single first-order equation:

$$\frac{1}{\rho^2} \frac{d}{d\rho} [\rho(1-f)] = K(\rho) \quad \Rightarrow \quad \frac{dm}{d\rho} = \frac{\rho^2}{2} K(\rho), \quad (2.10)$$

where the dimensionless mass function $m(\rho)$ is defined by $f(\rho) = 1 - 2m(\rho)/\rho$, and $K(\rho)$ is the energy density in dimensionless form. For the PINLED Y^n black holes discussed here, the solution for the lapse function is written in a parametric representation with $y = -Y/\mathfrak{E}^2$ as a parameter:

$$\begin{cases} f(y) = 1 - \frac{2m(y)}{\rho(y)} \\ \rho(y) = \left(\frac{2q^2}{y(1+y^{n-1})^3} \right)^{1/4}, \end{cases} \quad (2.11)$$

after we also transformed the second equation of (2.10) to an equation for $m(y)$ using the explicit expression for the dimensionless energy density $K(y)$:

$$K(y) = \frac{y}{4} + \frac{3n-2}{4n}y^n. \quad (2.12)$$

The solution for the mass function is given by

$$m(y) = \frac{q^{3/2}}{2^{1/4} \cdot 15(n-1)} \left[\frac{n(17n-49) + (10 + n(27n-101))y^{n-1} - 32ny^{2(n-1)}}{4n(1+y^{n-1})^{9/4}} y^{1/4} + \frac{8}{y^{(n-2)/4}} F\left(\frac{1}{4}, \frac{n-2}{4(n-1)}, \frac{5n-6}{4(n-1)}, -\frac{1}{y^{n-1}}\right) \right] + m_{\text{BH}} - \bar{m}_{\text{field}}, \quad (2.13)$$

where $F(a, b, c, z)$ is the hypergeometric function, m_{BH} is the black hole mass and \bar{m}_{field} is the (finite) total accumulated field mass in all space. This field mass is expressed as

$$\bar{m}_{\text{field}} = \frac{2^{3/4}q^{3/2}}{3} \cdot \frac{\Gamma\left(\frac{4n-3}{4(n-1)}\right)\Gamma\left(\frac{5n-6}{4(n-1)}\right)}{\Gamma\left(\frac{9}{4}\right)}. \quad (2.14)$$

In Fig. (1) and (2), one can see the profiles of the lapse function and the horizon ρ_H as a function of m_{BH} with different values of q and n . PINLED Y^n black holes exhibit Schwarzschild-like (S-like) solutions (with one horizon) for small charges, and Reissner–Nordström-like (RN-like) solutions (with two horizons), for larger charges. The lower branches of the RN-like curves of Fig. (2) correspond to the inner horizons. The more relevant to this paper is the event horizon which is the exterior if the number of horizons is larger than 1. Thus we will usually refer to the event horizon simply as “horizon” and take some care when distinction is needed. For larger n , the critical charge leading to naked singularities decreases. As expected, for fixed BH mass the charge q always reduces the horizon radius, while for fixed charge the mass increases the horizon radius.

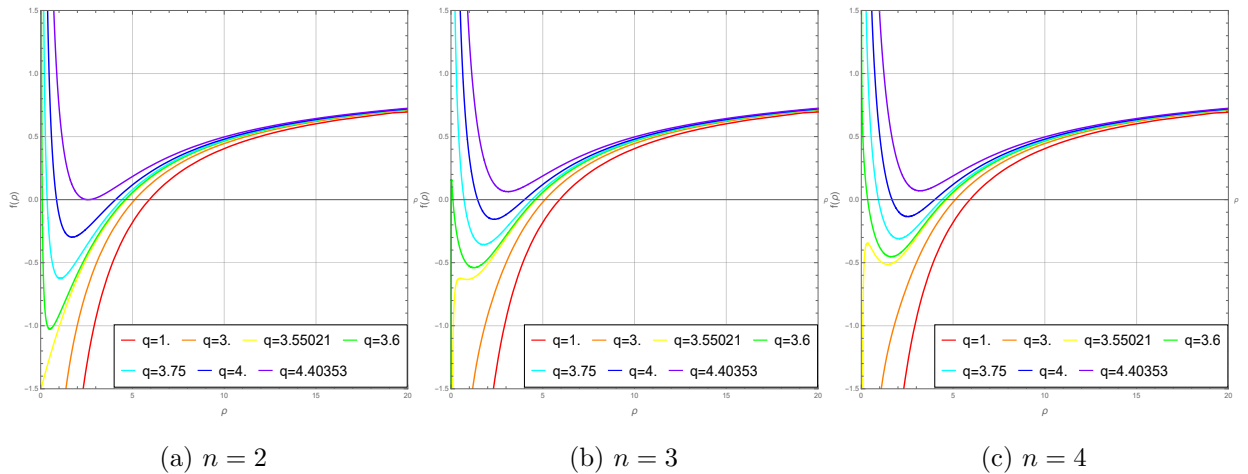


Figure 1: Lapse function $f(\rho)$ of BH solutions of the PINLED Y^n model with various values of q for n values $n = 2, 3, 4$ with $m_{\text{BH}} = 3$.

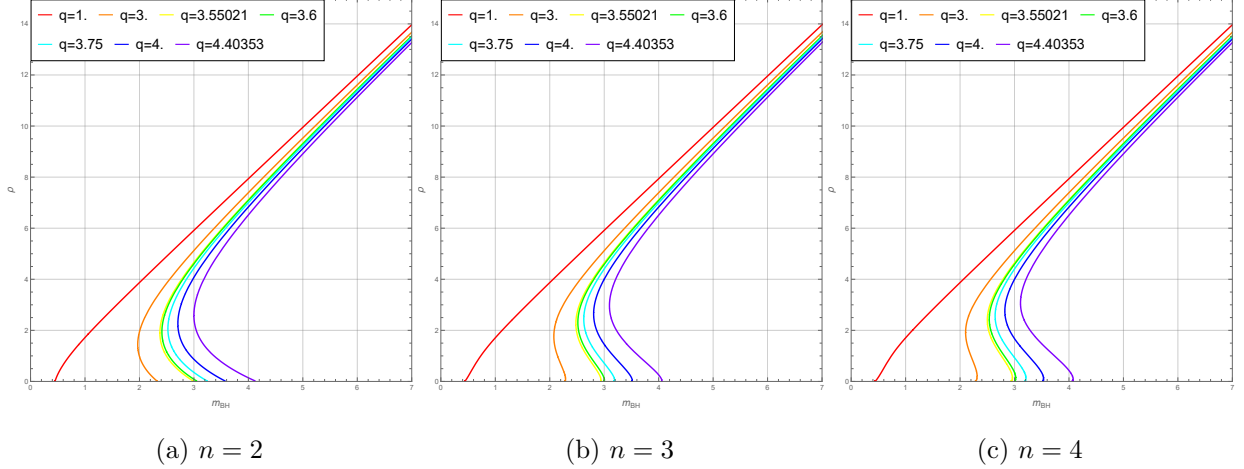


Figure 2: Horizon radius ρ_H versus black hole mass m_{BH} for Y^n BHs with various values of q for $n = 2, 3, 4$. Notice that $q = 4.40353$ is the critical q for $m_{BH} = 3$ and $n = 2$, which corresponds to

a naked singularity for $n = 3$ and 4.

III. TIMELIKE AND NULL GEODESICS AROUND Y^n BLACK HOLES

For the study of timelike and null geodesics around the Y^n BHs we will follow the standard procedure by first, writing the geodesic equation and identifying the constants of motion in the equatorial plane $\theta = \pi/2$. To this end, we define the Lagrangian as $\mathcal{L}_p = \Lambda/2$, where

$$\Lambda = -g_{\mu\nu}\dot{x}^\mu\dot{x}^\nu = -f(\rho)\dot{t}^2 + \frac{\dot{\rho}^2}{f(\rho)} + \rho^2\dot{\phi}^2. \quad (3.1)$$

where the dot represents the derivative with respect to an affine parameter. This Lagrangian immediately yields two conserved quantities: the energy $E = f(\rho)\dot{t}$ and the angular momentum $L = \rho^2\dot{\phi}$. The Lagrangian itself is also constant along geodesics, $\Lambda = -\xi$. By an affine transformation, we can choose $\xi = \{1, 0\}$ for massive and massless particles, respectively. This allows us to write the radial equation in the form of a one-dimensional mechanical energy equation for a point particle:

$$\dot{\rho}^2 + V_{\text{eff}} = E^2, \quad (3.2)$$

where the effective potential is given by

$$V_{\text{eff}} = f(\rho) \left(\frac{L^2}{\rho^2} + \xi \right). \quad (3.3)$$

It is also useful to use an analogous mechanical equation for the geometry of the trajectories $r(\phi)$:

$$\left(\frac{d\rho}{d\phi} \right)^2 + W_{\text{eff}}(\rho) = 0, \quad (3.4)$$

where the new effective potential is

$$W_{\text{eff}} = \rho^2 f(\rho) + \frac{\rho^4}{L^2} (\xi f(\rho) - E^2). \quad (3.5)$$

Notice the structural difference of this mechanical equation with respect to the previous one: the particle energy is an additional parameter in the effective potential, while the effective energy always vanishes.

Now let us investigate massive and massless cases.

A. Massive Neutral Particles ($\xi = 1$)

First, we discuss the simplest types of orbits around the black hole, namely timelike circular orbits. For these, the radial velocity must vanish, $\dot{\rho}(t) = 0$ for all t , which corresponds to $V_{\text{eff}} = E^2$ and $V'_{\text{eff}}(\rho) = 0$. Stable circular orbits exist if $V''_{\text{eff}}(\rho) > 0$ and the limiting case of this family of orbits is the *innermost stable circular orbit* (ISCO), which is determined by the additional condition of marginal stability, $V''_{\text{eff}}(\rho) = 0$. From $V'_{\text{eff}}(\rho) = 0$ we obtain the following explicit condition for circular orbits:

$$V'_{\text{eff}}(\rho) = \frac{L^2 (1 - 3f(\rho) - \rho^2 K(\rho))}{\rho^3} + \frac{\xi (1 - f(\rho) - \rho^2 K(\rho))}{\rho} = 0, \quad (3.6)$$

where we have used the field equation (2.10) for eliminating $f'(\rho)$ from the equation.

For the stability condition we need also the second derivative

$$V''_{\text{eff}}(\rho) = \frac{L^2 (12f(\rho) - \rho^3 K'(\rho) + 4\rho^2 K(\rho) - 6)}{\rho^4} - \frac{\xi (2(1 - f(\rho)) + \rho^3 K'(\rho))}{\rho^2}, \quad (3.7)$$

which as mentioned above should be positive. The ISCO is the limiting case of marginal stability which occurs for $V''_{\text{eff}}(\rho) = 0$ in addition to (3.6). Solving Eq. (3.6) for the angular momentum (which is possible only for $\xi \neq 0$) and substituting in (3.7), we obtain a single equation that determines the ISCO radius ρ_i :

$$V''_{\text{eff}}(\rho_i) = 2\xi \frac{f(\rho_i) (3f(\rho_i) + \rho_i^3 K'(\rho_i) + 7\rho_i^2 K(\rho_i) - 5) + 2(1 - \rho_i^2 K(\rho_i))^2}{\rho_i^2 (-3f(\rho_i) - \rho_i^2 K(\rho_i) + 1)} = 0 \quad (3.8)$$

An equivalent equation can be obtained by recognizing that the ISCO radius corresponds to the minimum of the angular momentum function obtained by solving Eq. (3.6) as mentioned above. The ISCO radius thus obtained, is independent of the orbit parameters (like L and E). It depends only on the BH characteristics, n , q and m_{BH} .

Since for our Y^n BHs, the radial dependence of all quantities is not explicit, but is given in a parametric form using the additional radial relation $\rho(y)$ of (2.11), all the quantities in this equation

are actually functions of y , or should be expressed as such, like $K'(\rho) = dK/d\rho$ using the explicit form (2.12) for $K(y)$. After doing that, one solves Eq. (3.8) with respect to y_i , the parametric value corresponding to the ISCO, and then obtain the associated ISCO radius as $\rho_i = \rho(y_i)$.

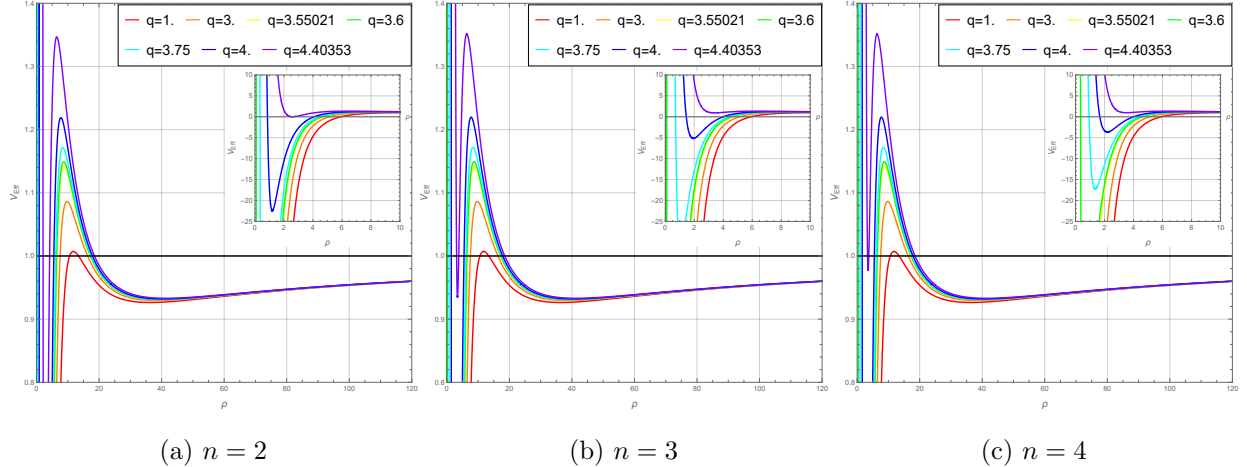


Figure 3: Effective potential for massive particles ($\xi = 1$) vs radius ρ for Y^n BHs with various values of q for n values 2,3 and 4 with $m_{BH} = 3$ and $L = 4m_{BH}$. Notice that the next to largest zero of $V_{\text{eff}}(\rho)$ is at the event horizon, and that the minimum of $V_{\text{eff}}(\rho)$ which is relevant to the circular orbits and ISCO is the shallow one further to the right around $\rho = 40$ in these plots.

In Fig. (3) we have plotted the effective potential for massive particles with a given angular momentum for different cases. We observe that depending on the nonlinearity parameter n and charge q one has a different nontrivial orbital structure. For low charge values (up to $q = 3$) we have a Schwarzschild like behavior, a single infinitely deep potential well near the horizon and a second shallow binding potential relatively far from the horizon. Beyond these lower values, we have an intermediary state where we see the development of a double minima structure with the interior one fully inside the horizon. In this configuration there emerges a potential barrier between the inner and outer wells. As charge increases, both potential wells become shallower, as the black hole's grip on photons weakens since repulsive electromagnetic effects dominates.

Furthermore, in Figs. 4 and 5 we present the behavior of the ISCO radius as a function of the BH mass and charge, respectively. The overall trends can be read off directly from the figures, or from the numerical results summarized in Table I for small q and m_{BH} . Increasing m_{BH} at fixed q shifts ρ_{ISCO} outward, consistent with the expectation that a more massive black hole extends the range of its gravitational influence. Similarly, increasing q at fixed m_{BH} shifts the ISCO inward, suggesting that in the PINLED framework the electromagnetic contribution to gravity effectively

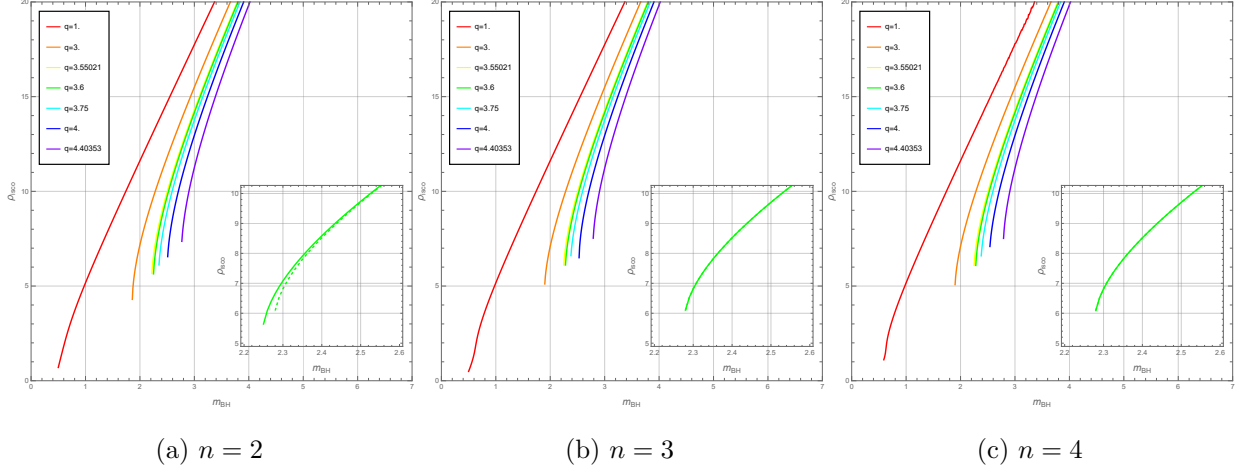


Figure 4: ISCO radius for massive particles ($\xi = 1$) as a function of the BH mass m_{BH} for the Y^n BHs, shown for various values of the charge q and for $n = 2, 3$, and 4. In the inset panel, dashed curve correspond to the Reissner–Nordström (RN) case. For $n = 3$ and 4, the difference between the PINLED and RN results becomes indistinguishable even in smaller scales.

diminishes the net attractive potential, driving ρ_{ISCO} to smaller values. We compare the PINLED results with the Reissner–Nordström (RN) limit where for the comparison we write the RN lapse as

$$f_{\text{RN}}(y) = 1 - \frac{2m_{\text{BH}}}{\rho(y)} + \frac{q^2}{2\rho^2(y)}, \quad (3.9)$$

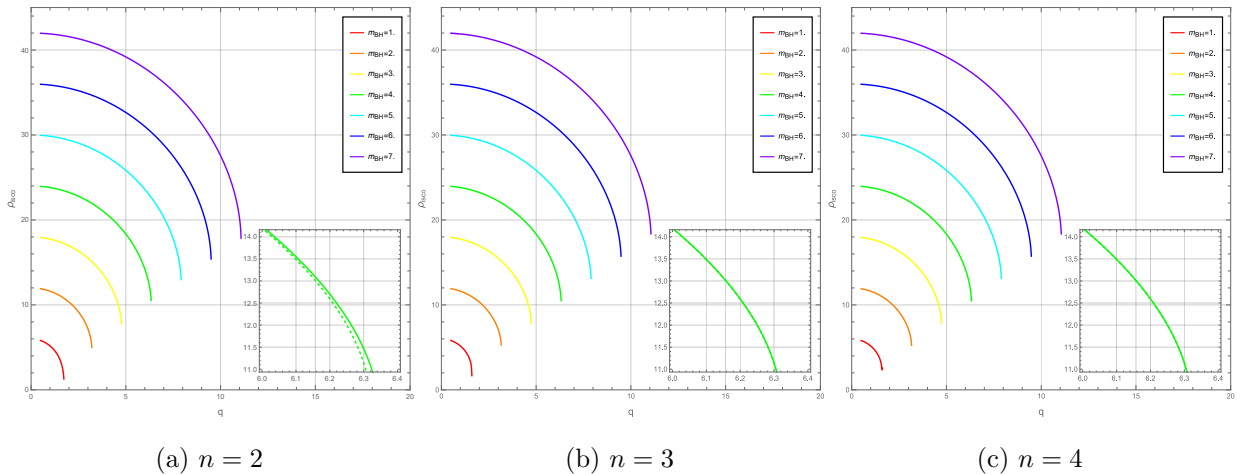


Figure 5: ISCO radius for massive particles ($\xi = 1$) as a function of the charge q for the Y^n BHs with various fixed values of the BH mass m_{BH} and for $n = 2, 3$, and 4. In the inset panel the dashed curve represent the corresponding RN results.

using the same parametric representation of the radial coordinate $\rho(y)$ defined in Eq. (2.11). For the RN case we employ the same ISCO criterion based on Eq.(3.8) with $f_{\text{RN}}(y)$ given above and $K_{\text{RN}}(y) = y/4$.

We find that the two families of ISCO curves are very close to each other, with deviations being most pronounced at $n = 2$ and small charge and mass, and becoming progressively smaller as n increases to 3 and 4. By $n = 3$ and 4, the Y^n curves are virtually indistinguishable from the RN ones even at finer scales, as confirmed by the inset panels in Figs. 4 and 5. This convergence indicates that the nonlinear corrections encoded in the Y^n model become increasingly suppressed at higher n for ρ_{ISCO} , rendering this parameter an unfavorable probe for differentiating Y^n from RN BHs. The results in Table I confirm this quantitatively: for instance, at $q = 0.1$ and $m_{\text{BH}} = 0.2$, the Y^n value decreases from 1.16229 at $n = 2$ to 1.16163 at $n = 4$, converging toward the RN value of 1.16163, while at larger charges such as $q = 0.3$, the deviation is more pronounced at $n = 2$ but similarly converges by $n = 4$.

In the next sections we will see that massless particles are more likely to tell Y^n BHs apart from RN ones, since they can “penetrate” closer to the BH horizons, i.e. to the regions where the differences between the metric tensors of both kinds of BHs are more noticeable. Still, the deviations of the Y^n BHs with respect to the RN ones will diminish with increasing charge and mass.

q	RN			PINLED ($n = 2$)		
	$m_{\text{BH}} = 0.2$	$m_{\text{BH}} = 0.3$	$m_{\text{BH}} = 0.4$	$m_{\text{BH}} = 0.2$	$m_{\text{BH}} = 0.3$	$m_{\text{BH}} = 0.4$
0.1	1.16163	1.77475	2.38115	1.16229	1.77483	2.38116
0.2	1.03329	1.69570	2.32326	1.04793	1.69729	2.32360
0.3	0.709808	1.54994	2.22182	0.862759	1.56128	2.22392
q	PINLED ($n = 3$)			PINLED ($n = 4$)		
	$m_{\text{BH}} = 0.2$	$m_{\text{BH}} = 0.3$	$m_{\text{BH}} = 0.4$	$m_{\text{BH}} = 0.2$	$m_{\text{BH}} = 0.3$	$m_{\text{BH}} = 0.4$
0.1	1.16164	1.77475	2.38115	1.16163	1.77475	2.38115
0.2	1.03463	1.69572	2.32326	1.03339	1.69570	2.32326
0.3	0.804013	1.55035	2.22184	0.775924	1.54995	2.22182

Table I: ISCO values for PINLED Y^n black holes and RN metric for low q and m_{BH} range.

B. Massless Particles $\xi = 0$

In this subsection, we focus on the motion of massless (neutral) particles moving along null geodesics, such as photons. This is done by setting $\xi = 0$ in Eqs.(3.3) and (3.5), which simplifies the effective potential to

$$V_{\text{eff}} = f(\rho) \left(\frac{L^2}{\rho^2} \right), \quad (3.10)$$

as well as the associated effective potential for light rays (i.e. $r(\phi)$) to

$$W_{\text{eff}} = \rho^2 f(\rho) - \rho^4/b^2 \quad (3.11)$$

where $b = L/E$ is the impact parameter of a light ray. In what follows we will use both kinds of effective potential according to our convenience.

Depending on the profile of the effective potential $V_{\text{eff}}(\rho)$, it can exhibit both minima and maxima corresponding to stable and unstable circular orbits, respectively. The potential for massless particles typically admits both, but outside the horizon there are only unstable circular orbits. These orbits occur at the photon sphere (or photon ring in 2+1 dimensions), where the centrifugal repulsion is exactly balanced by the gravitational attraction.

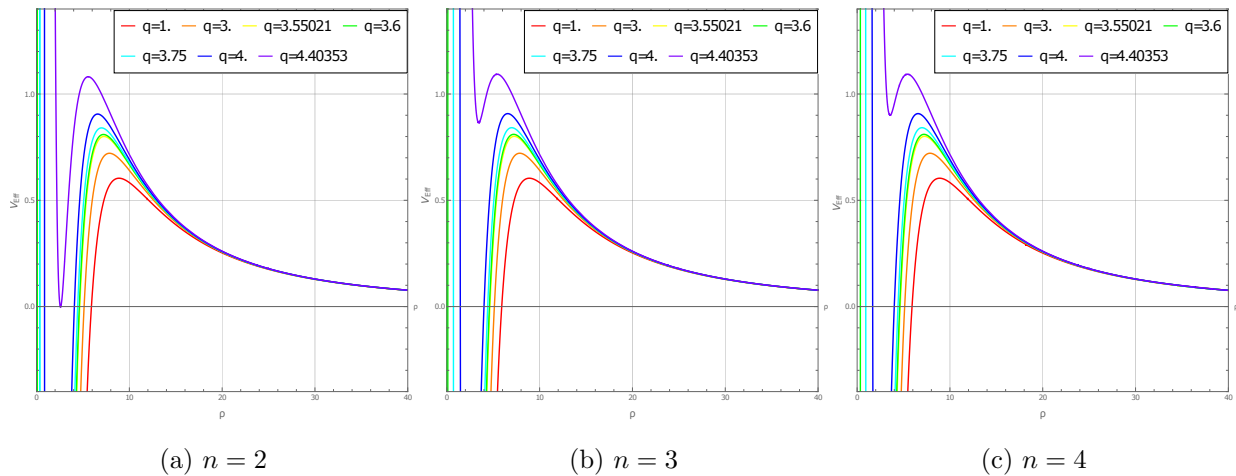


Figure 6: Effective potential $V_{\text{eff}}(\rho)$ for massless particles ($\xi = 0$) for Y^n BHs with various values of q for n values 2,3 and 4 with $m_{BH} = 3$. The photon spheres correspond to the static unstable $\rho(\lambda)$ “sitting” at the top of the potential hill.

In Fig. 6 we can see the profile of effective potential $V_{\text{eff}}(\rho)$ of Y^n black holes for various values of n with a given angular momentum. The minima that correspond to stable photon orbits are hidden behind horizon which is located at the exterior root of $V_{\text{eff}}(\rho)$. Furthermore as expected,

we observe an evolution from a Schwarzschild like profile (low q) to a more oscillatory profile with additional turning point as q increases.

The condition for circular null geodesics is obtained by requiring that the radial acceleration vanishes, which is equivalent to extremizing the effective potential $dV_{\text{eff}}/d\rho = 0$ as we saw already for massive particles. For the potential (3.10) for null geodesics this yields

$$V'_{\text{eff}} = \frac{L^2}{\rho^3}(\rho f'(\rho) - 2f(\rho)) = 0. \quad \Rightarrow \quad \rho_{ps} f'(\rho_{ps}) = 2f(\rho_{ps}) \quad (3.12)$$

Furthermore, using the field equation (2.10) we may eliminate $f'(\rho)$ and obtain a simple algebraic relation for the photon sphere radius ρ_{ps} , which can be also be obtained directly from the RHS of (3.6) with $\xi = 0$:

$$1 - 3f(\rho_{ps}) - \rho_{ps}^2 K(\rho_{ps}) = 0. \quad (3.13)$$

More useful for our Y^n solutions which utilize parametric representation, is (3.13) rewritten in terms of y , or its alternative version written in terms of y and the mass function:

$$\frac{6m(y_{ps})}{\rho(y_{ps})} - \rho^2(y_{ps})K(y_{ps}) - 2 = 0. \quad (3.14)$$

For given solutions y_{ps} of Eq. (3.14) one can obtain the corresponding photon sphere radius ρ_{ps} with the condition $\rho_{ps} > \rho_H$. We note that like the ISCO radius, the photon sphere radius is

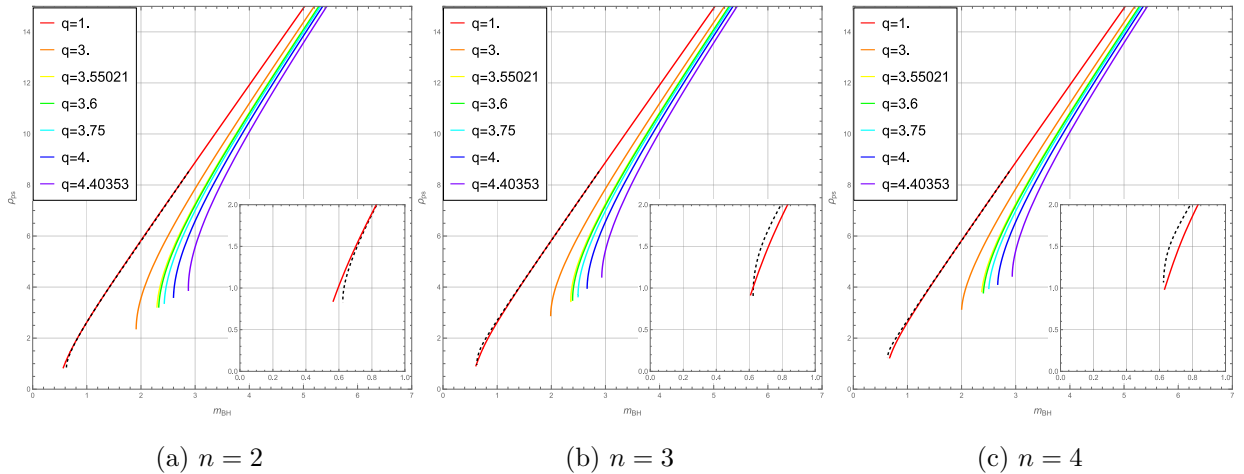


Figure 7: Photon sphere radius ρ_{ps} as a function of the black hole mass m_{BH} for the Y^n black hole with various values of the charge q and for $n = 2, 3$, and 4. Black dashed curves represent the corresponding RN case with $q = 1$ for each value of n . Other parameter choices yield similar qualitative behavior.

independent of the specific orbital parameters, but depends only on the BH characteristics, n , q and m_{BH} .

In Fig. (7), the dependence of the photon sphere radius ρ_{ps} on the black hole mass m_{BH} is displayed for various charge parameters q and nonlinearity parameter n . The solid curves represent the Y^n BH photon sphere radii, while the dashed curves which split from the lower parts of the solid curves correspond to the RN BHs for the charge values $q = 1$. All ρ_{ps} profiles with fixed charge increase monotonically with m_{BH} . For a given m_{BH} , increasing the charge q leads to a systematic decrease of ρ_{ps} reflecting the repulsive PINLED contribution to the effective gravitational pull. The overall behavior remains qualitatively similar for different n , though larger n slightly modifies the profiles.

Complementarily, in Fig. (8) the variation of ρ_{ps} with q is shown for several fixed black hole masses. For a given mass, ρ_{ps} decreases monotonically as the charge increases. For larger masses, the photon sphere radius is correspondingly greater, consistent with the stronger gravitational influence of more massive black holes. The qualitative behavior remains similar across different n values, with increasing n producing only minor quantitative shifts in the curves.

In both Figs. (7) and (8), we observe that the photon sphere radius ρ_{ps} in the Y^n and RN spacetimes exhibits qualitatively similar behavior over most of the parameter space. Noticeable deviations arise primarily in the low-mass and high-charge (near-extremal) regime, where the values of ρ_{ps} differ between the two models. In particular, for $n = 2$ the RN photon sphere radius is smaller

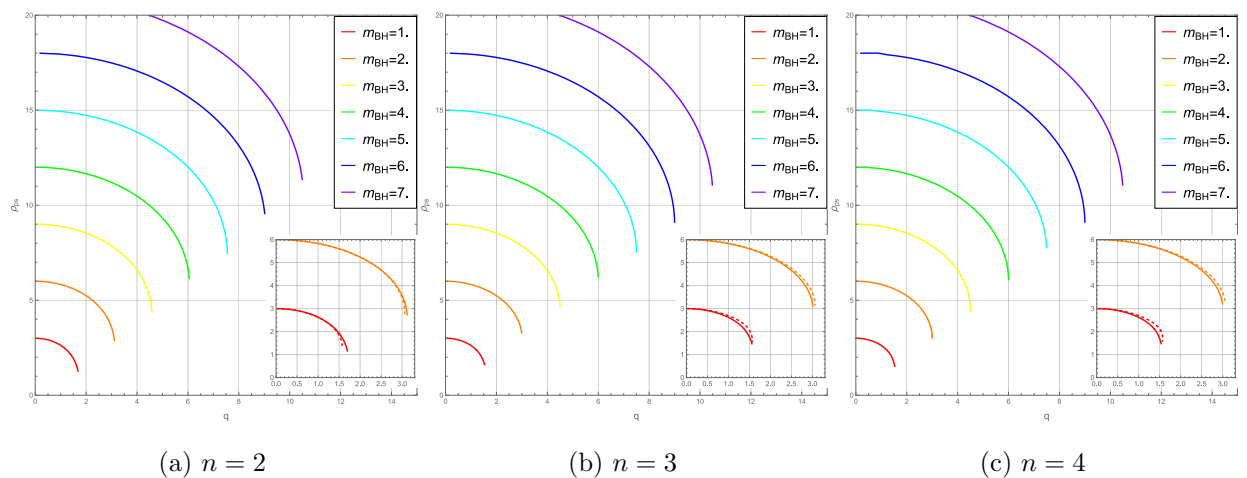


Figure 8: Photon sphere radius ρ_{ps} as a function of the charge q for the Y^n black hole with various fixed values of the black hole mass m_{BH} and for $n = 2, 3$, and 4. Dashed curves represent the corresponding RN results. Other parameter choices yield similar qualitative behavior.

than its Y^n counterpart, whereas for higher values of n the Reissner–Nordström radius becomes larger in this regime.

C. Shadow Radius

In the era of very-long-baseline interferometry (VLBI), which gave us the first images of the supermassive black holes M87* and SgrA*, the concept of the black hole "shadow" has become a central observable in testing strong-field gravity. The shadow is not the event horizon itself, but a dark silhouette cast against the bright, lensed background emission of the surrounding accretion flow. This silhouette appears because photons with sufficiently small impact parameters fall into the black hole, creating a region of photon capture. The boundary of this dark region is defined by the critical photon orbits.

For a distant observer, the shadow is a circular (or nearly circular) disk whose apparent radius is governed by the innermost photon orbits. A key quantity for describing these orbits is the impact parameter $b = L/E$ defined already at the previous subsection. As we have shown there, unstable photon circular orbits exist at a critical radius ρ_{ps} . The corresponding critical impact parameter b_{crit} separates photons that fall into the black hole from those that escape to infinity. In asymptotically flat spacetimes, this critical impact parameter directly corresponds to the shadow radius r_s observed at infinity. For our spherically-symmetric line element (2.9), we can easily relate the shadow radius to the photon sphere quantities. For that we notice that the critical light rays that arrive at the observer are those which connect the photon sphere and the observer represented by the ray shown in Fig. 9. The angle α between such a light ray and the radial direction at the

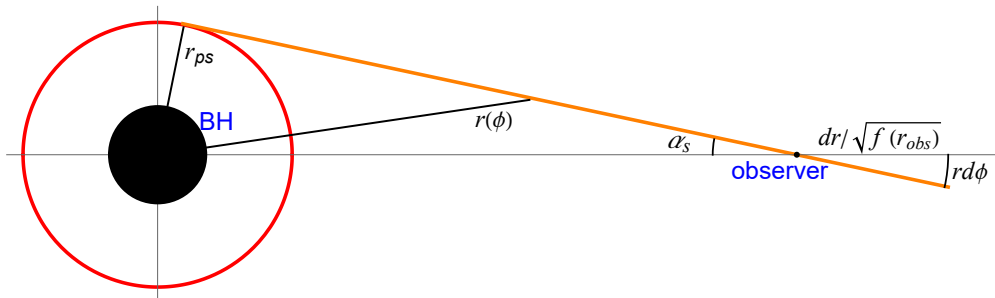


Figure 9: Illustration of shadow calculation from the observer's position r_{obs} . The shadow angle α_s is the angle between the limiting light ray (which arrives from the photon sphere (radius r_{ps}) at the observer) and the radial direction. The infinitesimal angular and radial lengths are calculated at $r = r_{obs}$.

location of the observer satisfies the following relation written in terms of the dimensionless radial variable:

$$\cot^2 \alpha = \left(\frac{d\rho/\sqrt{f(\rho_{obs})}}{\rho_{obs} d\phi} \right)^2 = \frac{1}{\rho_{obs}^2 f(\rho_{obs})} \left(\frac{d\rho}{d\phi} \right)^2 \Big|_{\rho=\rho_{obs}} = \frac{-W_{\text{eff}}(\rho_{obs})}{\rho_{obs}^2 f(\rho_{obs})} \quad (3.15)$$

where for the last term we used Eq.(3.4). Actually, this expression is still valid for any light ray which arrives at the observer. In order to specify in light rays which connect the observer with

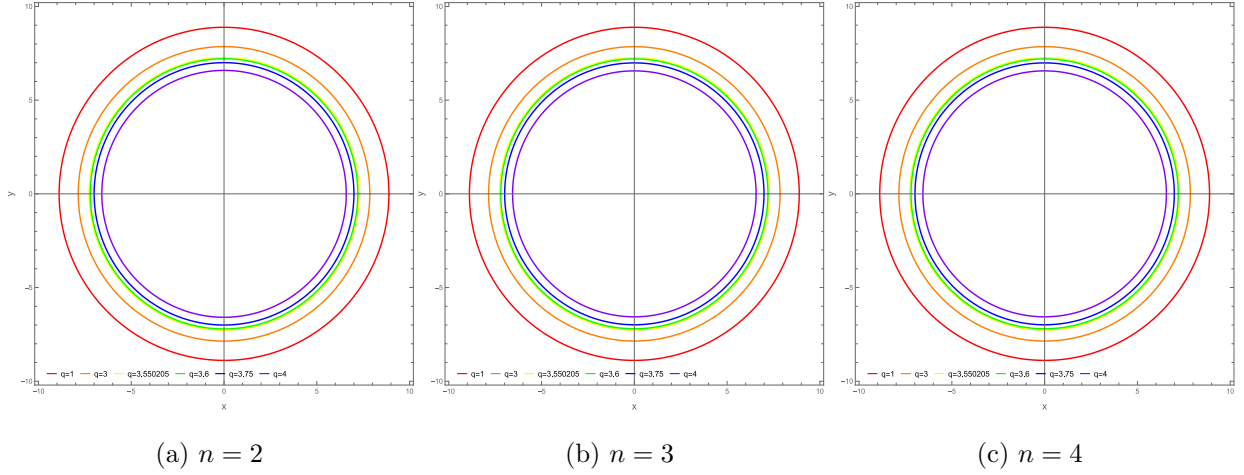


Figure 10: Shadow values for Y^n BH with various values of charge q for n values 2,3 and 4 for $m_{BH} = 3$.

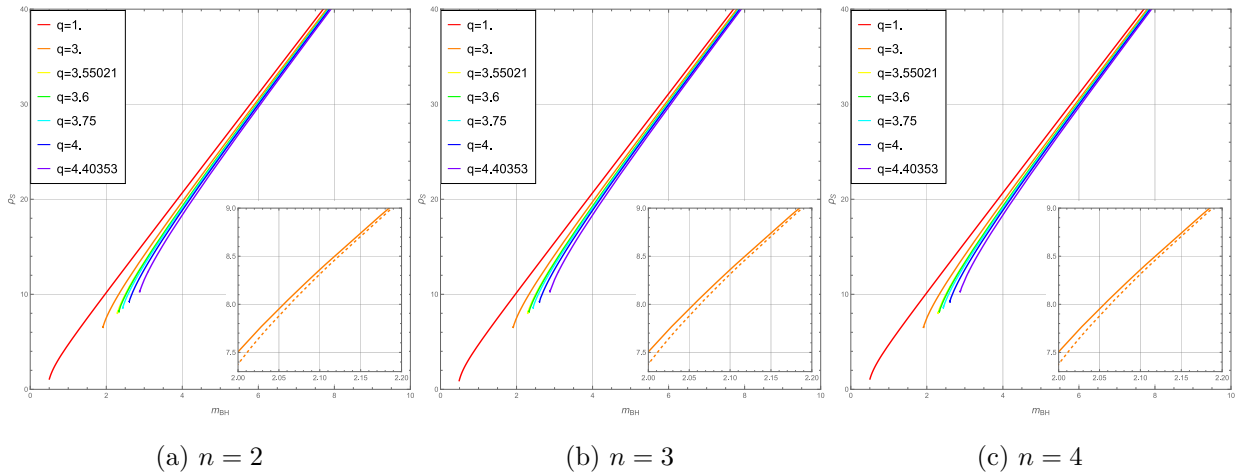


Figure 11: Shadow radius ρ_s as a function of the black hole mass m_{BH} for the Y^n black hole with various values of the charge q and for $n = 2, 3$, and 4. Dashed curve denote the corresponding RN result for the same charge value. Other choices of q exhibit similar qualitative behavior.

the photon sphere, we need to pick up the impact parameter b_{crit} which yields $W_{eff}(\rho_{ps}) = 0$ and use that value in $W_{eff}(\rho_{obs})$. Looking at the relevant expression (3.11), we find immediately that $b_{crit}^2 = \rho_{obs}^2 / f(\rho_{obs})$, and by substituting in (3.15) we obtain:

$$\sin^2 \alpha_s = \frac{\rho_{ps}^2}{f(\rho_{ps})} \frac{f(\rho_{obs})}{\rho_{obs}^2}. \quad (3.16)$$

The radius of the BH shadow for an observer at a large distance can be obtained using Eq.(3.16) as

$$\rho_s \simeq \rho_{obs} \sin \alpha_s \simeq \frac{\rho_{ps}}{\sqrt{f(\rho_{ps})}} \sqrt{f(\rho_{obs})}, \quad (3.17)$$

so the shadow radius as perceived by a static observer at infinity is given by:

$$\rho_s = \frac{\rho_{ps}}{\sqrt{f(\rho_{ps})}} \quad (3.18)$$

In the context of PINLED model, using (3.13) we obtain the expression for the shadow radius as

$$\rho_s = \frac{\sqrt{3}\rho(y_{ps})}{\sqrt{1 - \rho^2(y_{ps})K(y_{ps})}} \quad (3.19)$$

for use in parametric representation.

Figure (10) shows the calculated shadow radius for the Y^n black holes as a geometric diagram. It is evident that the shadow radius decreases systematically with increasing charge q . Figure (11) illustrates the dependence of the shadow radius ρ_s on the black hole mass m_{BH} , where ρ_s increases

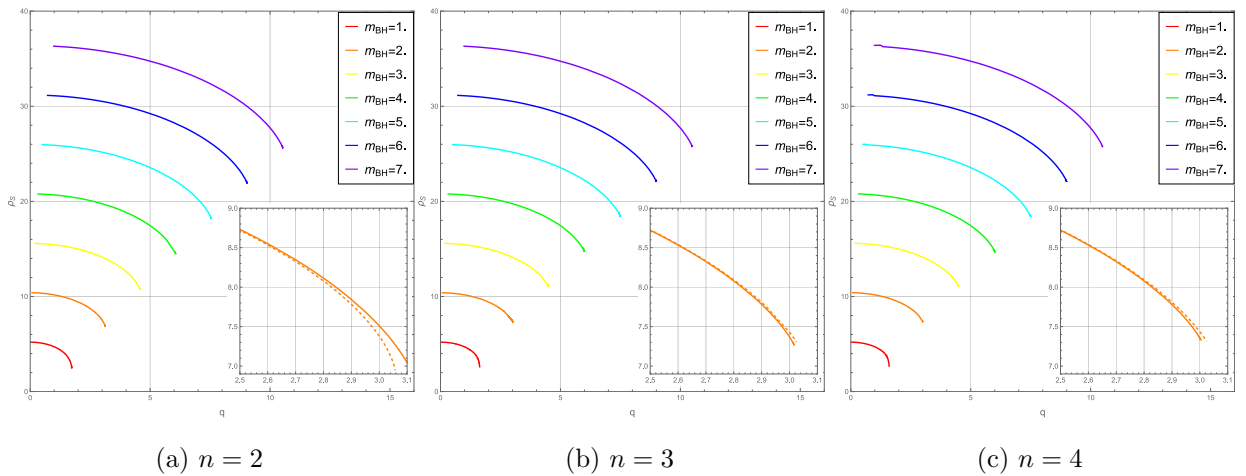


Figure 12: Shadow radius ρ_s as a function of the charge q for various values of the black hole mass m_{BH} and for $n = 2, 3$, and 4 . Dashed curve denote the corresponding RN result for the same mass value. Other parameter choices exhibit similar qualitative behavior.

monotonically as m_{BH} grows. Finally, Fig. (12) presents the behavior of ρ_s as a function of q for a fixed mass, again exhibiting a decrease with increasing charge up to a critical value. Overall, the differences between the PINLED and RN models remain small in the shadow observables, but more pronounced for small masses, while increasing with charge.

IV. LIGHT DEFLECTION ANGLES

In this section we will turn to unbound trajectories and analyze light deflection resulting by PINLED Y^n BHs. The trajectories of a photon moving in a static, spherically symmetric spacetime can be conveniently analyzed using orbital equation (3.4) with the effective potential (3.11)

$$\left(\frac{d\rho}{d\phi}\right)^2 + \rho^2 f(\rho) - \frac{\rho^4}{b^2} = 0 \quad (4.1)$$

where $b = L/E$. The turning point of the trajectory corresponds to the point of closest approach ρ_m , where the radial component of the photon's four-velocity vanishes. Thus, by applying Eq. (4.1) to $\rho = \rho_m$ we obtain the following relation among ρ_m and b :

$$\left(\frac{d\rho}{d\phi}\right)^2 \Big|_{\rho=\rho_m} = 0 \quad \Rightarrow \quad \frac{1}{b^2} = \frac{f(\rho_m)}{\rho_m^2}. \quad (4.2)$$

Therefore, we can use this relation to calculate first the asymptotic direction of a light ray with respect to the direction of its closest approach, which we are free to choose as $\phi = 0$:

$$\Delta\phi = \int_{\rho_m}^{\infty} \frac{d\rho}{\sqrt{\frac{\rho^4}{\rho_m^2} f(\rho_m) - \rho^2 f(\rho)}} \quad (4.3)$$

for a trajectory symmetric about the point of closest approach, the deflection angle δ of a light ray with respect to its asymptotic incoming direction, can be written as

$$\delta = 2\Delta\phi - \pi \quad (4.4)$$

As always, the integral for $\Delta\phi$ in (4.4) should be calculated for deflection by Y^n BHs after the change of variables $\rho(y)$. The deflection angle is specific to the light trajectory characterized by ρ_m , or alternatively by the impact parameter b . Fig. (13) illustrates the variation of the deflection angle δ (in radians) as a function of the closest approach distance ρ_m for light deflection by the Y^n BHs, considering different nonlinearity orders $n = 2, 3$ and 4. The results are compared with the Schwarzschild and RN cases, shown, respectively, by the dashed and solid black curves, for a fixed black hole mass $m_{\text{BH}} = 3$.

As expected, the deflection angle increases sharply as ρ_m approaches the photon sphere radius ρ_{ps} , where the light rays winds around the BH with increasingly large number of times. Since the photon sphere radii depend on the BH parameters, each curve has a different divergence point. For larger and increasing ρ_m , the deflection angle decreases monotonically, and all curves converge to the weak deflection regime where $\delta \rightarrow 0$ asymptotically. Increasing the charge q leads to a stronger deviation from the Schwarzschild curve, reducing the deflection angle at a given ρ_m . This reflects the repulsive PINLED contribution to the effective gravitational pull, which effectively weakens the light deflection by Y^n BHs. However, a comparison with the RN case shows that the deflection angle remains essentially unchanged at high charge values, while deviations becoming appreciable for sufficiently small charges. We also note that the difference between the two curves of the deflection angle increases while approaching from large distances to the photon sphere. This is also consistent with the observation that the departure of Y^n metric tensor from the RN one, also increases towards the center.

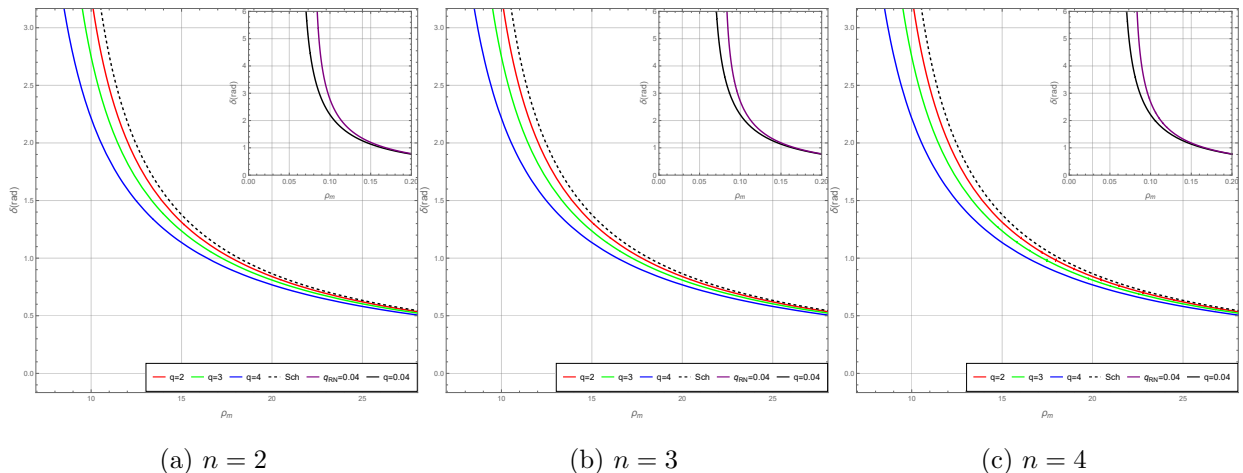


Figure 13: Light deflection angle δ (in radians) vs closest approach ρ_m for $m_{BH} = 3$ and various q values. Dashed black lines represent Schwarzschild ($q = 0$) case. The inserts present a comparison between RN (black) and Y^n (purple) cases, both with small charge and mass values where the difference is visible: $q = 0.04$, $m_{BH} = 0.03$.

V. PERIASTRON PRECESSION

In this section, we present a general and systematic derivation of the periastron precession within the PINLED model. We focus on the motion of massive test particles, corresponding to the substitution $\xi = 1$ in Eqs (3.3) and (3.5). Eqs. (3.4) and (3.5) consist together the first order

“mechanical” equation which determines the geometrical shape of the orbits $\rho(\phi)$. The equation for massive test particles is:

$$\left(\frac{d\rho}{d\phi}\right)^2 = -\rho^2 f(\rho) - \frac{\rho^4}{L^2} f(\rho) + \frac{E^2}{L^2} \rho^4 \equiv -W(\rho), \quad (5.1)$$

where we denote here by $W(\rho)$ the effective potential with $\xi = 1$. For studying the periastron precession we focus on bound (but not necessarily closed) orbits. The two radial turning points of these orbits are determined by the condition $W(\rho) = 0$. These roots define the extrema of the radial motion, with ρ_- corresponding to the periastron and ρ_+ to the apastron.

The angular displacement accumulated as the particle moves from the periastron to the apastron is obtained by integrating $d\phi/d\rho$ using the explicit Eq.(5.1), between the corresponding turning points. The total angular advance over one complete radial oscillation (periastron to apastron and back) is therefore given by

$$\Phi = 2 \int_{\rho_-}^{\rho_+} \frac{d\rho}{\sqrt{-W(\rho)}}, \quad (5.2)$$

For a closed (periodic) Keplerian orbit one would have $\Phi = 2\pi$; any deviation from this value signals the presence of periastron precession. Accordingly, the periastron shift per orbit is defined as

$$\delta\phi = \Phi - 2\pi = 2 \int_{\rho_-}^{\rho_+} \frac{d\rho}{\sqrt{-W(\rho)}} - 2\pi. \quad (5.3)$$

Notice that the integration limits ρ_- and ρ_+ are determined by the orbit parameters: energy E and angular momentum L . This is done from the two solutions of the equation $W(\rho_{\pm}) = 0$ mentioned above. However, it is easier to do the converse and solve the same equations for E and L in terms of ρ_- and ρ_+ . The result is:

$$E^2 = \frac{f(\rho_-)f(\rho_+) (\rho_-^2 - \rho_+^2)}{f(\rho_+)\rho_-^2 - f(\rho_-)\rho_+^2}, \quad L^2 = \frac{[f(\rho_-) - f(\rho_+)] \rho_-^2 \rho_+^2}{f(\rho_+)\rho_-^2 - f(\rho_-)\rho_+^2}, \quad (5.4)$$

For a given orbital configuration specified by the turning points ρ_- and ρ_+ , these expressions allow the conserved quantities to be determined uniquely. Substituting Eq. (5.4) into Eq. (5.3), one can compute the periastron precession for any bound orbit in any static, spherically symmetric spacetime characterized by a lapse function $f(\rho)$. In the present context of PINLED Y^n BHs, we have to adapt these results for the parametric representation that we are using. This is done in a straightforward way by the change of variables $\rho(y)$ in the integration in Eq. (5.3) together with changing the integration limits from ρ_- and ρ_+ to their corresponding values y_- and y_+ .

Fig. 14 displays the periastron precession $\delta\phi$ for Y^n black holes as a function of the periastron radius ρ_- , black hole mass m_{BH} and charge q with fixed apastron ρ_+ . In Fig. 14a $\delta\phi$ decreases

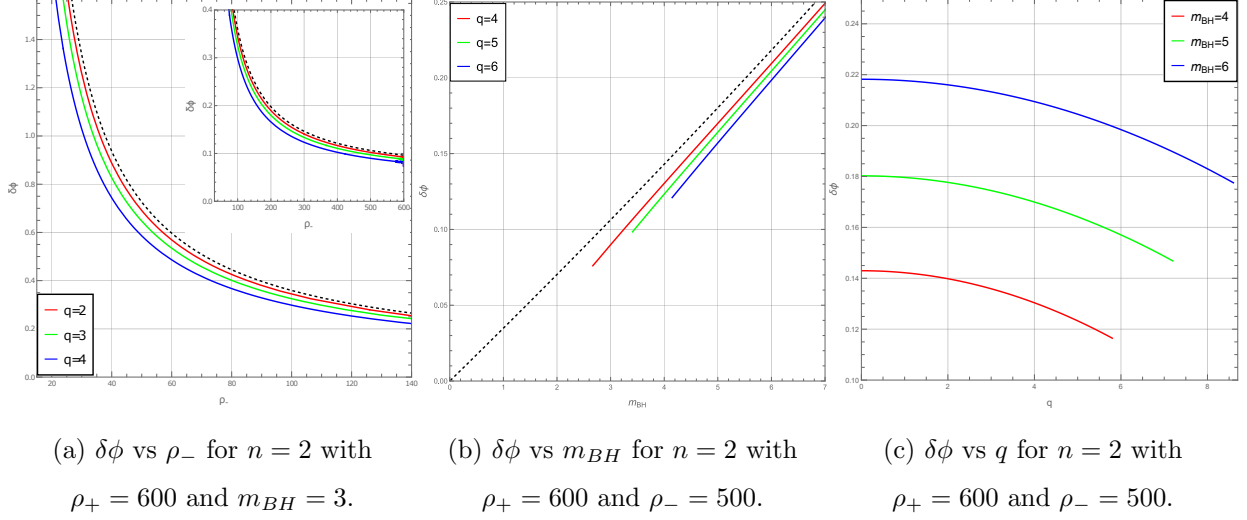


Figure 14: Periastron precession $\delta\phi$ as a function of the periastron radius ρ_- , mass m_{BH} and the charge parameter q for Y^n BHs for fixed apastron values. The black dashed curves in Fig. 14a and 14b correspond to the Schwarzschild BHs, and the $q = 0$ values of the curves on the vertical axis in Fig. 14c represent the Schwarzschild precession values with the corresponding m_{BH} .

monotonically with respect to ρ_- for fixed m_{BH} and several values of q . Increasing q yields smaller precession for fixed ρ_- . We notice that at the end points of the curves which correspond to circular orbits, $\delta\phi$ does not vanish. This is a well-known peculiarity of the precession angle. Fig. 14b shows that $\delta\phi$ grows with m_{BH} similarly to the Schwarzschild case, nearly linear in m_{BH} for fixed q . The three curves for different q values remain closely spaced, so demonstrating that the charge contribution is a subdominant correction to the mass term, since for fixed q , the mass can grow

q	RN			PINLED ($n = 2$)		
	$m_{BH} = 3$	$m_{BH} = 4$	$m_{BH} = 5$	$m_{BH} = 3$	$m_{BH} = 4$	$m_{BH} = 5$
1	0.10528	0.14218	0.17961	0.10528	0.14217	0.17960
3	0.09707	0.13588	0.17445	0.09705	0.13587	0.17445
4	0.08987	0.13036	0.16994	0.08986	0.13034	0.16994
q	PINLED ($n = 3$)			PINLED ($n = 4$)		
	$m_{BH} = 3$	$m_{BH} = 4$	$m_{BH} = 5$	$m_{BH} = 3$	$m_{BH} = 4$	$m_{BH} = 5$
1	0.10524	0.14214	0.17957	0.10523	0.14213	0.17956
3	0.09677	0.13588	0.17445	0.09667	0.13545	0.17401
4	0.08938	0.12981	0.16936	0.08922	0.12963	0.16917

Table II: Periastron precession $\delta\phi$ for various values of n , q and m_{BH} for $\rho_- = 500$ and $\rho_+ = 600$.

indefinitely and the metric becomes closer to Schwarzschild. On the other hand, the charge value has a bound of the order of m_{BH} . Fig. 14c illustrates the dependence on q at fixed m_{BH} and ρ_- where the precession decreases gradually with increasing q . This is qualitatively in line with the RN result, where the charge introduces a retrograde correction to the precession angle. For the higher n -values, $n = 3$ and $n = 4$, the precession results are indistinguishable from the $n = 2$ case within the resolution of the plot. Table II compares the periastron precession between the RN and PINLED models for the same ρ_+ and ρ_- across various values of n, q and m_{BH} . One can see a systematic deviation in PINLED values that grows with both n and q . In all cases $\delta\phi$ increases with m_{BH} and decreases with q .

VI. CONCLUSION

In this work our main aim was to provide a systematic and self-contained set of strong and weak field observables for the static, spherically symmetric PINLED- Y^n black-hole solutions minimally coupled to Einstein-Hilbert gravity. Motivated by the EHT era, where photon-ring/shadow measurements and precision lensing tests increasingly probe the near-horizon geometry, we analyzed null and timelike geodesics in the spacetime (2.9) (with the metric function given by parametric representation (2.11) with (2.13)+(2.14)), and quantified how the charge parameter q and the non-linearity index n deform the photon sphere, the shadow size, and the characteristic radii governing massive particle motion like the ISCO and perihelion precession angle.

For timelike geodesics, we determined circular orbits and the ISCO from $V'_{\text{eff}} = 0$ and $V''_{\text{eff}} = 0$, obtaining the compact condition (3.8) and solving it for ρ_{ISCO} as a function of mass, charge and the

q	$n = 2$				$n = 3$				$n = 4$			
	ρ_H	ρ_{ISCO}	ρ_{ps}	ρ_s	ρ_H	ρ_{ISCO}	ρ_{ps}	ρ_s	ρ_H	ρ_{ISCO}	ρ_{ps}	ρ_s
1	5.9155	17.7475	8.8875	15.4425	5.91548	17.7475	8.88748	15.4425	5.91548	17.7475	8.88748	15.4425
3	5.12662	15.5007	7.85661	14.1304	5.12137	15.4993	7.85411	14.12880	5.12132	15.4993	7.8541	14.1288
3.55021	4.66136	14.2943	7.27317	13.4144	4.64298	14.2903	7.26519	13.4095	4.64258	14.2903	7.26515	13.4096
3.6	4.60883	14.1652	7.20899	13.3372	4.58796	14.1608	7.20005	13.3318	4.58747	14.1608	7.2	13.3318
3.75	4.4355	13.7219	7.00031	13.0887	4.40414	13.7158	6.98756	13.0811	4.40316	13.7157	6.98747	13.0811
4	4.07624	12.9592	6.58674	12.6095	4.00442	12.9484	6.56181	12.5953	4.0003	12.9484	6.56156	13.0811

Table III: Characteristic radii ρ_H , ρ_{ISCO} , ρ_{ps} , and ρ_s for different values of the charge parameter q and nonlinearity index $n = 2, 3, 4$, computed for a fixed black hole mass $m_{BH} = 3$.

index n as showed in subsection III A. Table III demonstrates that ρ_{ISCO} decreases with increasing q over the parameter range displayed, tracking the contraction of the characteristic strong field region and providing an additional, independent probe of the geometry. Since the ISCO sets a key scale for accretion dynamics (e.g., the inner edge of thin disks and the onset of strong-field orbital shear), these shifts translate into potentially observable changes in disk spectra and variability when PINLED corrections are appreciable. In short, both in null and timelike geodesics, we see the inherent electromagnetic repulsive effect.

Our results show that, for fixed black hole mass, increasing the charge parameter q shifts the characteristic radii inward: the horizon radius ρ_H , the photon sphere radius ρ_{ps} , the shadow radius ρ_s , and the ISCO radius ρ_{ISCO} all decrease as q grows. This behavior is consistent with the fact that the nonlinear electromagnetic sector reduces the net attractive pull relative to the Schwarzschild case. Conversely, for fixed q , these radii increase with m_{BH} , as expected from the stronger gravitational field of a more massive source.

Another outcome of our analysis is that null-geodesic observables showed in subsection III B and III C provide a probe of departures from the Reissner-Nordström geometry. provide the clearest probe of departures from the Reissner-Nordström geometry. In particular, both ρ_{ps} and ρ_s decrease monotonically with q , while the differences between the PINLED and RN cases become most visible in the low mass high charge regime. By contrast, the ISCO remains very close to the RN prediction over most of the parameter space explored here, especially for $n = 3$ and 4, indicating that timelike circular motion is a comparatively weak discriminator of the nonlinear PINLED corrections. The dependence on the nonlinearity index n is generally subleading compared with the dependence on q . Although increasing n produces small quantitative shifts in the characteristic radii, these corrections remain modest, and for several observables the $n = 3$ and $n = 4$ cases become nearly indistinguishable from the RN limit. This indicates that, within the present family of solutions, the charge parameter is the dominant control parameter for the optical and orbital structure, while the effect of the nonlinear index is comparatively mild.

We also analyzed light deflection in section IV and periastron precession in section V. As usual, the light deflection weakens as the light ray closest approach increases. For fixed closest-approach distance, fixed BH mass and increasing charge, the light deflection angle decreases from the maximum of the Schwarzschild value in the zero-charge limit, while its dependence on n remains weak. The deviation of light deflection for Y^n BHs with respect to RN is minute in the weak field - large ρ_m values. It becomes distinguishable in the opposite limit where ρ_m gets closer to the photon sphere and especially for small BH masses. Likewise, for bound particle orbits with fixed turning

points, the periastron advance increases with m_{BH} but decreases with q , again with only small corrections induced by changing n . These particle observables, ISCO and especially the periastron precession provide useful consistency checks, but they are less sensitive to the PINLED deformation than the quantities associated with the photon region.

Overall, our results furnish a coherent set of strong and weak field calculations for this new class of first-order nonlinear-electrodynamics black holes. They show that the most promising signatures of the PINLED- Y^n geometry are encoded in null-geodesic observables, especially the photon sphere and the shadow, whereas timelike circular motion and weak field tests mainly provide secondary constraints. Natural extensions of this work include rotating PINLED solutions, quasinormal-mode and ringdown analyses, and the incorporation of realistic emission models and radiative-transfer effects for direct comparison with horizon-scale observations.

ACKNOWLEDGMENTS

İ.İ.Ç. and Y.V. would like to thank for financial support by the Israeli fund for scientific regional cooperation and the Research Authority of the Open University of Israel. A. Ö. would like to acknowledge networking support of the COST Action CA21106 - COSMIC WISPerS in the Dark Universe: Theory, astrophysics and experiments (CosmicWISPerS), the COST Action CA22113 - Fundamental challenges in theoretical physics (THEORY-CHALLENGES), the COST Action CA21136 - Addressing observational tensions in cosmology with systematics and fundamental physics (CosmoVerse), the COST Action CA23130 - Bridging high and low energies in search of quantum gravity (BridgeQG), and the COST Action CA23115 - Relativistic Quantum Information (RQI) funded by COST (European Cooperation in Science and Technology). A. Ö. also thanks to EMU, TUBITAK, ULAKBIM (Turkiye) and SCOAP3 (Switzerland) for their support. Y.V. also thanks COST Action CA23130 - Bridging high and low energies in search of quantum gravity (BridgeQG).

-
- [1] R. Abuter *et al.* (GRAVITY), Detection of the Schwarzschild precession in the orbit of the star S2 near the Galactic centre massive black hole, *Astron. Astrophys.* **636**, L5 (2020), [arXiv:2004.07187 \[astro-ph.GA\]](#).
- [2] K. Akiyama *et al.* (Event Horizon Telescope), First M87 Event Horizon Telescope Results. I. The Shadow of the Supermassive Black Hole, *Astrophys. J. Lett.* **875**, L1 (2019), [arXiv:1906.11238 \[astro-](#)

- [ph.GA](#)].
- [3] K. Akiyama *et al.* (Event Horizon Telescope), First Sagittarius A* Event Horizon Telescope Results. I. The Shadow of the Supermassive Black Hole in the Center of the Milky Way, *Astrophys. J. Lett.* **930**, L12 (2022), [arXiv:2311.08680 \[astro-ph.HE\]](#).
 - [4] T. Johannsen and D. Psaltis, Testing the No-Hair Theorem with Observations in the Electromagnetic Spectrum: II. Black-Hole Images, *Astrophys. J.* **718**, 446 (2010), [arXiv:1005.1931 \[astro-ph.HE\]](#).
 - [5] A. E. Broderick, T. Johannsen, A. Loeb, and D. Psaltis, Testing the No-Hair Theorem with Event Horizon Telescope Observations of Sagittarius A*, *Astrophys. J.* **784**, 7 (2014), [arXiv:1311.5564 \[astro-ph.HE\]](#).
 - [6] T. Johannsen, A. E. Broderick, P. M. Plewa, S. Chatzopoulos, S. S. Doeleman, F. Eisenhauer, V. L. Fish, R. Genzel, O. Gerhard, and M. D. Johnson, Testing General Relativity with the Shadow Size of Sgr A*, *Phys. Rev. Lett.* **116**, 031101 (2016), [arXiv:1512.02640 \[astro-ph.GA\]](#).
 - [7] C. Bambi, Testing black hole candidates with electromagnetic radiation, *Rev. Mod. Phys.* **89**, 025001 (2017), [arXiv:1509.03884 \[gr-qc\]](#).
 - [8] Z. Younsi, A. Zhidenko, L. Rezzolla, R. Konoplya, and Y. Mizuno, New method for shadow calculations: Application to parametrized axisymmetric black holes, *Phys. Rev. D* **94**, 084025 (2016), [arXiv:1607.05767 \[gr-qc\]](#).
 - [9] A. Grenzebach, V. Perlick, and C. Lämmerzahl, Photon Regions and Shadows of Kerr-Newman-NUT Black Holes with a Cosmological Constant, *Phys. Rev. D* **89**, 124004 (2014), [arXiv:1403.5234 \[gr-qc\]](#).
 - [10] R. A. Hennigar, M. B. J. Poshteh, and R. B. Mann, Shadows, Signals, and Stability in Einsteinian Cubic Gravity, *Phys. Rev. D* **97**, 064041 (2018), [arXiv:1801.03223 \[gr-qc\]](#).
 - [11] X.-M. Kuang, Z.-Y. Tang, B. Wang, and A. Wang, Constraining a modified gravity theory in strong gravitational lensing and black hole shadow observations, *Phys. Rev. D* **106**, 064012 (2022), [arXiv:2206.05878 \[gr-qc\]](#).
 - [12] T. Bronzwaer and H. Falcke, The Nature of Black Hole Shadows, *Astrophys. J.* **920**, 155 (2021), [arXiv:2108.03966 \[astro-ph.HE\]](#).
 - [13] S. Vagnozzi, C. Bambi, and L. Visinelli, Concerns regarding the use of black hole shadows as standard rulers, *Class. Quant. Grav.* **37**, 087001 (2020), [arXiv:2001.02986 \[gr-qc\]](#).
 - [14] Y. Chen, R. Roy, S. Vagnozzi, and L. Visinelli, Superradiant evolution of the shadow and photon ring of Sgr A*, *Phys. Rev. D* **106**, 043021 (2022), [arXiv:2205.06238 \[astro-ph.HE\]](#).
 - [15] S. Boyeneni, J. Wu, and E. R. Most, Unveiling the Electrodynamical Nature of Spacetime Collisions, *Phys. Rev. Lett.* **135**, 101401 (2025), [arXiv:2504.15978 \[gr-qc\]](#).
 - [16] J. L. Synge, The Escape of Photons from Gravitationally Intense Stars, *Mon. Not. Roy. Astron. Soc.* **131**, 463 (1966).
 - [17] V. Perlick and O. Y. Tsupko, Calculating black hole shadows: Review of analytical studies, *Phys. Rept.* **947**, 1 (2022), [arXiv:2105.07101 \[gr-qc\]](#).
 - [18] P. V. P. Cunha and C. A. R. Herdeiro, Shadows and strong gravitational lensing: a brief review, *Gen.*

- Rel. Grav. **50**, 42 (2018), [arXiv:1801.00860 \[gr-qc\]](#).
- [19] V. Bozza, Gravitational lensing in the strong field limit, *Phys. Rev. D* **66**, 103001 (2002), [arXiv:gr-qc/0208075](#).
- [20] K. S. Virbhadra and G. F. R. Ellis, Schwarzschild black hole lensing, *Phys. Rev. D* **62**, 084003 (2000), [arXiv:astro-ph/9904193](#).
- [21] C.-M. Claudel, K. S. Virbhadra, and G. F. R. Ellis, The Geometry of photon surfaces, *J. Math. Phys.* **42**, 818 (2001), [arXiv:gr-qc/0005050](#).
- [22] K. S. Virbhadra, Relativistic images of Schwarzschild black hole lensing, *Phys. Rev. D* **79**, 083004 (2009), [arXiv:0810.2109 \[gr-qc\]](#).
- [23] S. Capozziello, E. Battista, and S. De Bianchi, Null geodesics, causal structure, and matter accretion in Lorentzian-Euclidean black holes, *Phys. Rev. D* **112**, 044009 (2025), [arXiv:2507.08431 \[gr-qc\]](#).
- [24] S. E. Gralla, D. E. Holz, and R. M. Wald, Black Hole Shadows, Photon Rings, and Lensing Rings, *Phys. Rev. D* **100**, 024018 (2019), [arXiv:1906.00873 \[astro-ph.HE\]](#).
- [25] G. Lambiase, D. J. Gogoi, R. C. Pantig, and A. Övgün, Shadow and quasinormal modes of the rotating Einstein–Euler–Heisenberg black holes, *Phys. Dark Univ.* **48**, 101886 (2025), [arXiv:2406.18300 \[gr-qc\]](#).
- [26] A. Uniyal, S. Chakrabarti, R. C. Pantig, and A. Övgün, Nonlinearly charged black holes: Shadow and thin-accretion disk, *New Astron.* **111**, 102249 (2024), [arXiv:2303.07174 \[gr-qc\]](#).
- [27] M. Born and L. Infeld, Foundations of the new field theory, *Proc. Roy. Soc. Lond. A* **144**, 425 (1934).
- [28] H. Euler and B. Kockel, The scattering of light by light in Dirac’s theory, *Naturwiss* **23**, 246 (1933).
- [29] W. Heisenberg and H. Euler, Consequences of Dirac’s theory of positrons, *Z. Phys.* **98**, 714 (1936), [arXiv:physics/0605038](#).
- [30] D. P. Sorokin, Introductory Notes on Non-linear Electrodynamics and its Applications, *Fortsch. Phys.* **70**, 2200092 (2022), [arXiv:2112.12118 \[hep-th\]](#).
- [31] M. Novello, S. E. Perez Bergliaffa, and J. M. Salim, Singularities in general relativity coupled to nonlinear electrodynamics, *Class. Quant. Grav.* **17**, 3821 (2000), [arXiv:gr-qc/0003052](#).
- [32] G. W. Gibbons and C. A. R. Herdeiro, Born-Infeld theory and stringy causality, *Phys. Rev. D* **63**, 064006 (2001), [arXiv:hep-th/0008052](#).
- [33] H. A. Gonzalez, M. Hassaine, and C. Martinez, Thermodynamics of charged black holes with a nonlinear electrodynamics source, *Phys. Rev. D* **80**, 104008 (2009), [arXiv:0909.1365 \[hep-th\]](#).
- [34] B. Toshmatov, Z. Stuchlík, J. Schee, and B. Ahmedov, Electromagnetic perturbations of black holes in general relativity coupled to nonlinear electrodynamics, *Phys. Rev. D* **97**, 084058 (2018), [arXiv:1805.00240 \[gr-qc\]](#).
- [35] T. Harada, Neutron stars in scalar tensor theories of gravity and catastrophe theory, *Phys. Rev. D* **57**, 4802 (1998), [arXiv:gr-qc/9801049](#).
- [36] E. Ayon-Beato and A. Garcia, Regular black hole in general relativity coupled to nonlinear electrodynamics, *Phys. Rev. Lett.* **80**, 5056 (1998), [arXiv:gr-qc/9911046](#).
- [37] E. Ayon-Beato and A. Garcia, The Bardeen model as a nonlinear magnetic monopole, *Phys. Lett. B*

- [493](#), 149 (2000), [arXiv:gr-qc/0009077](#).
- [38] E. Ayon-Beato and A. Garcia, New regular black hole solution from nonlinear electrodynamics, *Phys. Lett. B* **464**, 25 (1999), [arXiv:hep-th/9911174](#).
- [39] K. A. Bronnikov, Regular magnetic black holes and monopoles from nonlinear electrodynamics, *Phys. Rev. D* **63**, 044005 (2001), [arXiv:gr-qc/0006014](#).
- [40] I. Dymnikova, Regular electrically charged structures in nonlinear electrodynamics coupled to general relativity, *Class. Quant. Grav.* **21**, 4417 (2004), [arXiv:gr-qc/0407072](#).
- [41] L. Balart and E. C. Vagenas, Regular black holes with a nonlinear electrodynamics source, *Phys. Rev. D* **90**, 124045 (2014), [arXiv:1408.0306 \[gr-qc\]](#).
- [42] Z.-Y. Fan and X. Wang, Construction of Regular Black Holes in General Relativity, *Phys. Rev. D* **94**, 124027 (2016), [arXiv:1610.02636 \[gr-qc\]](#).
- [43] M. Hassaine and C. Martinez, Higher-dimensional charged black holes solutions with a nonlinear electrodynamics source, *Class. Quant. Grav.* **25**, 195023 (2008), [arXiv:0803.2946 \[hep-th\]](#).
- [44] H. Maeda, M. Hassaine, and C. Martinez, Lovelock black holes with a nonlinear Maxwell field, *Phys. Rev. D* **79**, 044012 (2009), [arXiv:0812.2038 \[gr-qc\]](#).
- [45] M. Cataldo and A. Garcia, Three dimensional black hole coupled to the Born-Infeld electrodynamics, *Phys. Lett. B* **456**, 28 (1999), [arXiv:hep-th/9903257](#).
- [46] M. Cataldo and A. Garcia, Regular (2+1)-dimensional black holes within nonlinear electrodynamics, *Phys. Rev. D* **61**, 084003 (2000), [arXiv:hep-th/0004177](#).
- [47] G. W. Gibbons and D. A. Rasheed, Electric - magnetic duality rotations in nonlinear electrodynamics, *Nucl. Phys. B* **454**, 185 (1995), [arXiv:hep-th/9506035](#).
- [48] G. W. Gibbons and D. A. Rasheed, $Sl(2, \mathbb{R})$ invariance of nonlinear electrodynamics coupled to an axion and a dilaton, *Phys. Lett. B* **365**, 46 (1996), [arXiv:hep-th/9509141](#).
- [49] M. Novello, V. A. De Lorenci, J. M. Salim, and R. Klippert, Geometrical aspects of light propagation in nonlinear electrodynamics, *Phys. Rev. D* **61**, 045001 (2000), [arXiv:gr-qc/9911085](#).
- [50] V. A. De Lorenci, R. Klippert, M. Novello, and J. M. Salim, Light propagation in nonlinear electrodynamics, *Phys. Lett. B* **482**, 134 (2000), [arXiv:gr-qc/0005049](#).
- [51] E. F. Eiroa, Gravitational lensing by Einstein-Born-Infeld black holes, *Phys. Rev. D* **73**, 043002 (2006), [arXiv:gr-qc/0511065](#).
- [52] V. Perlick, O. Y. Tsupko, and G. S. Bisnovatyi-Kogan, Influence of a plasma on the shadow of a spherically symmetric black hole, *Phys. Rev. D* **92**, 104031 (2015), [arXiv:1507.04217 \[gr-qc\]](#).
- [53] S. G. Ghosh, A nonsingular rotating black hole, *Eur. Phys. J. C* **75**, 532 (2015), [arXiv:1408.5668 \[gr-qc\]](#).
- [54] B. Toshmatov, Z. Stuchlík, and B. Ahmedov, Generic rotating regular black holes in general relativity coupled to nonlinear electrodynamics, *Phys. Rev. D* **95**, 084037 (2017), [arXiv:1704.07300 \[gr-qc\]](#).
- [55] I. Dymnikova and E. Galaktionov, Regular rotating electrically charged black holes and solitons in non-linear electrodynamics minimally coupled to gravity, *Class. Quant. Grav.* **32**, 165015 (2015), [arXiv:1510.01353 \[gr-qc\]](#).

- [56] R. Kumar, A. Kumar, and S. G. Ghosh, Testing Rotating Regular Metrics as Candidates for Astrophysical Black Holes, *Astrophys. J.* **896**, 89 (2020), [arXiv:2006.09869 \[gr-qc\]](#).
- [57] B. Toshmatov, B. Ahmedov, and D. Malafarina, Can a light ray distinguish charge of a black hole in nonlinear electrodynamics?, *Phys. Rev. D* **103**, 024026 (2021), [arXiv:2101.05496 \[gr-qc\]](#).
- [58] K. Akiyama *et al.* (Event Horizon Telescope), First M87 Event Horizon Telescope Results. VI. The Shadow and Mass of the Central Black Hole, *Astrophys. J. Lett.* **875**, L6 (2019), [arXiv:1906.11243 \[astro-ph.GA\]](#).
- [59] P. Kocherlakota *et al.* (Event Horizon Telescope), Constraints on black-hole charges with the 2017 EHT observations of M87*, *Phys. Rev. D* **103**, 104047 (2021), [arXiv:2105.09343 \[gr-qc\]](#).
- [60] S. Vagnozzi *et al.*, Horizon-scale tests of gravity theories and fundamental physics from the Event Horizon Telescope image of Sagittarius A, *Class. Quant. Grav.* **40**, 165007 (2023), [arXiv:2205.07787 \[gr-qc\]](#).
- [61] A. Allahyari, M. Khodadi, S. Vagnozzi, and D. F. Mota, Magnetically charged black holes from nonlinear electrodynamics and the Event Horizon Telescope, *JCAP* **02**, 003, [arXiv:1912.08231 \[gr-qc\]](#).
- [62] P. V. P. Cunha and C. A. R. Herdeiro, Shadows and strong gravitational lensing: a brief review, *Gen. Rel. Grav.* **50**, 42 (2018), [arXiv:1801.00860 \[gr-qc\]](#).
- [63] M. Okyay and A. Övgün, Nonlinear electrodynamics effects on the black hole shadow, deflection angle, quasinormal modes and greybody factors, *JCAP* **01** (01), 009, [arXiv:2108.07766 \[gr-qc\]](#).
- [64] A. Uniyal, R. C. Pantig, and A. Övgün, Probing a non-linear electrodynamics black hole with thin accretion disk, shadow, and deflection angle with M87* and Sgr A* from EHT, *Phys. Dark Univ.* **40**, 101178 (2023), [arXiv:2205.11072 \[gr-qc\]](#).
- [65] G. J. Olmo and D. Rubiera-Garcia, Palatini $f(R)$ Black Holes in Nonlinear Electrodynamics, *Phys. Rev. D* **84**, 124059 (2011), [arXiv:1110.0850 \[gr-qc\]](#).
- [66] M. E. Rodrigues, E. L. B. Junior, G. T. Marques, and V. T. Zanchin, Regular black holes in $f(R)$ gravity coupled to nonlinear electrodynamics, *Phys. Rev. D* **94**, 024062 (2016), [Addendum: *Phys. Rev. D* **94**, 049904 (2016)], [arXiv:1511.00569 \[gr-qc\]](#).
- [67] M. E. Rodrigues and M. V. de Sousa Silva, Bardeen Regular Black Hole With an Electric Source, *JCAP* **06**, 025, [arXiv:1802.05095 \[gr-qc\]](#).
- [68] W. Berej, J. Matyjasek, D. Tryniecki, and M. Woronowicz, Regular black holes in quadratic gravity, *Gen. Rel. Grav.* **38**, 885 (2006), [arXiv:hep-th/0606185](#).
- [69] S. Capozziello, S. De Bianchi, and E. Battista, Avoiding singularities in Lorentzian-Euclidean black holes: The role of atemporality, *Phys. Rev. D* **109**, 104060 (2024), [arXiv:2404.17267 \[gr-qc\]](#).
- [70] S. Rasanen and Y. Verbin, Palatini formulation for gauge theory: implications for slow-roll inflation, *Open Journal of Astrophysics* **6**, 10.21105/astro.2211.15584 (2023), [arXiv:2211.15584 \[astro-ph.CO\]](#).
- [71] Y. Verbin, B. Pulice, A. Övgün, and H. Huang, New black hole solutions of second and first order formulations of nonlinear electrodynamics, *Phys. Rev. D* **111**, 084061 (2025), [arXiv:2412.20989 \[gr-qc\]](#).
- [72] J. Plebanski, Lectures on Non-Linear Electrodynamics, Nordita, Copenhagen (1970).